Journal of Electroanalytical Chemistry 920 (2022) 116611

Contents lists available at ScienceDirect

Journal of Electroanalytical Chemistry

journal homepage: www.elsevier.com/locate/jelechem

The effect of different carbon-based CdTe alloys for efficient photocatalytic glucose electrooxidation

Aykut Caglar [a,*], Omer Faruk Er [a], Nahit Aktas [a,d], Hilal Kivrak [b,c,*]

[a] Van Yuzuncu Yil University, Faculty of Engineering, Department of Chemical Engineering, Van, Turkey
[b] Eskisehir Osmangazi University, Faculty of Engineering and Architectural Sciences, Department of Chemical Engineering, Eskişehir, Turkey
[c] Translational Medicine Research and Clinical Center, Eskisehir Osmangazi University, Eskişehir, Turkey
[d] KyrgyzTurk Manas University, Faculty of Engineering, Department of Chemical Engineering, Bishkek, Kyrgyzstan

ARTICLE INFO

Keywords:
Cadmium
Carbon materials
Tellurium
Photocatalytic electrooxidation

ABSTRACT

The activated carbon (AC), graphene (G), reduced graphene oxide (rGO), carbon nanotube (CNT) supported CdTe photocatalysts at (50–50) atomic molar are synthesized by the sodium borohydride (SBH) method and characterized by the XRD, Micro-Raman, TEM-EDS, XPS, and TPx (TPR, TPO, and TPD) analyses. The CV, CA, and EIS electrochemical analyses are performed to investigate the catalytic activities of catalysts for photocatalytic glucose electrooxidation. Characterization analyses reveal that their electronic structures and surface properties change when carbon materials are doped with metal. The photocatalytic glucose electrooxidation results indicate that the 0.1 % CdTe(50–50)/CNT catalyst exhibited better photocatalytic activity, stability, and resistance than other catalysts both at dark (1.9 mA/cm^2) and under UV illumination (2.57 mA/cm^2). Therefore, the CNT-supported CdTe catalyst can be said a promising catalyst for direct glucose fuel cells.

1. Introduction

Energy is important for people to sustain their lives for heating, transportation, and many similar reasons. The world's energy needs are met from fossil fuels (natural gas, oil, coal) that harm nature [1]. When these fossil fuels burn, they release toxic gases such as CO_2, SO_x, and NO_x, causing harm to nature and the environment. In addition, it takes many years to renewable themselves. Therefore, researchers have shown great interest in alternative energy sources in recent years. Alternative energy sources include solar energy, wind energy, biomass energy, fuel cells. Fuel cells (FCs), a clean energy source and high-capacity energy systems, have attracted the interest of the scientific world to meet the world's energy needs as one of the most significant energy sources of the future. FCs are a sustainable and efficient energy source for a clean future that converts chemical energy directly into electrical energy [2–4]. Photoelectrochemical (PEC) cells have been recognized as one of the promising systems for solving the energy problem, thanks to which they make use of sunlight and produce electricity or chemical fuels [5,6]. Photocatalytic fuel cells (PFCs) that semiconductor photoanode, cathode, and electrolyte-containing such as methanol [7], ethanol [8], glucose ($C_6H_{12}O_6$) [9–12] are up-and-coming devices that could handle the energy needs and environmental pollution utilizing sunlight as energy input. Glucose is a high energy density (4.43 kWh/kg), non-toxic, flammable, and non-volatile, potential hydrogen carrier and is the most abundant simple sugar in nature [13]. A glucose molecule can produce 24 electrons and yield −2870 kJ/mol of energy via the complete oxidation to CO_2. However, glucose is a very stable molecule, it is difficult to break down and oxidize of C—H bond, so more research is needed. It is worth noting that it consists mostly of gluconic acid and a two-electron generating system, as demonstrated in the following chemical reaction in all studies to date [14]:

Anode: $C_6H_{12}O_6 + 2OH^- \rightarrow C_6H_{12}O_7$ (gluconic acid) $+ H_2O + 2e^-$ (4).

Cathode: $½O_2 + H_2O + 2e^- \rightarrow 2OH^-$ (5).

Overall: $C_6H_{12}O_6 + ½O_2 \rightarrow C_6H_{12}O_7 + 12H_2O$ (6).

Recently, the catalytic oxidation of glucose, which is utilized as a renewable energy source to meet the energy demand, was reported on metal-based carbon catalysts [2,15]. Caglar et al reported that they studied the photocatalytic glucose electrooxidation of C-TNT (9.1 mA/cm^2), Cd/TiO_2 (6 mA/cm^2), and CdSe/TiO_2 (7.2 mA/cm^2) catalysts [16–18]. Devadoss et al [19] reported glucose sensing and biohydrogen production in the direct photo-electrocatalytic oxidation of glucose with the Cu_2O-TiO_2 photocatalyst. They emphasized that

* Corresponding authors at: Eskisehir Osmangazi University, Faculty of Engineering and Architectural Sciences, Department of Chemical Engineering, Eskişehir, Turkey (H. Kivrak).
E-mail addresses: aykut_802@hotmail.com, aykut18.05.2015@gmail.com (A. Caglar), hilaldemir.kivrak@ogu.edu.tr (H. Kivrak).

https://doi.org/10.1016/j.jelechem.2022.116611
Received 9 March 2022; Received in revised form 8 June 2022; Accepted 8 July 2022
Available online 12 July 2022

Cu_2O–TiO_2 photoelectrodes could be used in biosensors and simultaneous biohydrogen production from direct photoelectrocatalytic oxidation of glucose. Yan et al [20] reported the glucose sensor and photoelectrochemical oxidation in an electrode modified with anatase TiO_2. They emphasized that it is important to develop applications of TiO_2-based catalysts in analytical chemistry and electrochemistry to improve the selectivity of the glucose sensor or the power density of fuel cells. Hamad et al [21] reported that they obtained 0.52 mA/cm^2 specific activity using an organic anode catalyst for glucose electrooxidation. In addition, PdIn/CNT (0.98 mA/cm^2) [22], PdAu/C (3 mA/cm^2) [23], NiO-TiO_2-ZrO_2/SO_4^{2-} (5.19 mA/cm^2) [24], Cu/Cu_2O/TNT (6.40 mA/cm^2) [25] materials were studied on glucose electrooxidation in literature.

Moreover, it is known that metal loading on the support plays an important role in determining the catalytic activity of catalysts in photocatalytic fuel cells. The metal loading on the support and the amount of metal affecting the thickness of the fuel cell catalyst layer also affect the cell performance. Literature studies have investigated the close relationship between metal loading, particle size, and catalyst layer thickness on the support and their effect on fuel cell performance. High metal loading on the support material reduces the interparticle distance, which affects the catalytic activity. Furthermore, the catalyst causes a decrease in surface area, thus leading to a decrease in catalytic activity [26,27].

Recently, the catalytic performance of catalysts has been examined in many fields such as water splitting [28], fuel cells [29–31], hydrogen storage [32], supercapacitors [33], solar energy [34], lithium-ion batteries [35] in the literature. However, photoanode catalysts developed for photocatalytic electrooxidation studies are not available in the literature except for a few studies. At present, AC, G, rGO, CNT supported CdTe photocatalysts were synthesized at (50:50) atomic molar by utilizing the SBH method. The XRD, Micro-Raman, TEM, XPS, and TPx (TPR, TPO, and TPD) analyses were used to examine the structure of catalysts. The CV, CA, and EIS analyses were realized to investigate the catalytic activity of photocatalytic glucose electrooxidation at dark and under UV illumination.

2. Experimental

2.1. Synthesis of supported-CdTe catalysts

All chemicals were bought from Sigma-Aldrich. CdTe(50–50) catalysts were synthesized with different support materials (AC, G, rGO, CNT) by using the SBH method. The Cd loading was adjusted to 0.1 % by the weight. Firstly, the appropriate amounts of Cd precursor and Te precursor were distributed under sonication with DI water in a beaker for 0.1 % CdTe(50–50)/CNT catalyst. After the metal precursors were homogeneously dispersed in DI water, CNT was added and mixed for about 120 min with both ultrasonic bath and mixer. Afterward, the reducing agent SBH was added dropwise into the solution. After mixing in both ultrasonic bath and mixer for 1 h, it was thoroughly washed with DI water and filtered. Finally, it was left to dry at 85 °C for overnight. All catalysts were synthesized under the same synthesis conditions.

2.2. Characterization of supported-CdTe catalysts

The X-ray Diffraction patterns (Empyrean (PANalytical) diffractometer) were performed to examine crystal structures of 0.1 % CdTe(50–50)/AC, G, rGO, CNT catalysts. TEM analysis of 0.1 % CdTe(50–50)/CNT catalyst was obtained using the Hitachi HighTech HT7700 device at 120 kV accelerating voltage and a maximum resolution of 0.204 nm. The elemental composition and oxidation state of the 0.1 % CdTe(50–50)/CNT catalyst were examined using XPS analysis (Specs-Flex) with a CCD detector (Kα (Al): 1486.7 eV). Micromeritics Chemisorb 2750 equipment was used to examine H_2-TPR, O_2-TPO, and NH_3-TPD analyses with an automated system attached by ChemiSoft TPx software.

2.3. Photo-electrochemical measurements

The CHI 660E potentiostat is a device used for electrochemical analysis. The CV, CA, and EIS analyses with this device were used to examine the catalytic activity, stability, and resistance of the catalysts, respectively. All analyses were performed in a three-electrode system with a reference electrode (Ag/AgCl), working electrode (Titanium metal), and counter electrode (Pt wire) with a scan rate of 100 mV/s at a potential range −0.65 V ~ 0.65 V in 1 M KOH and 1 M KOH + 0.5 M Glucose solution. The catalyst slurry was obtained from mixing CdTe(50–50)/AC, G, rGO, CNT catalysts and Nafion and it was transferred over titanium metal having 0.5 cm^2 area. The CV, CA, and EIS analyses were used to investigate catalytic activities of photocatalytic glucose electrooxidation at dark and under UV illumination. The UV lamp used for illumination had a power of 366 nm (long wavelength) and 6 W in a cabinet connected to the UVP device.

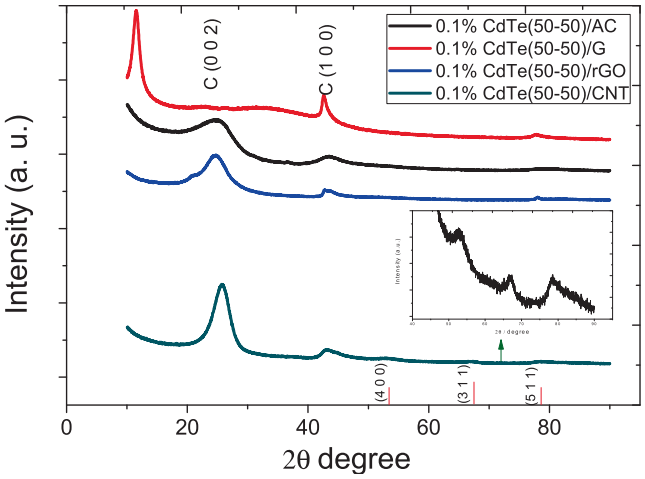

Fig. 1. XRD patterns of 0.1% CdTe(50–50)/AC, G, rGO, CNT catalysts.

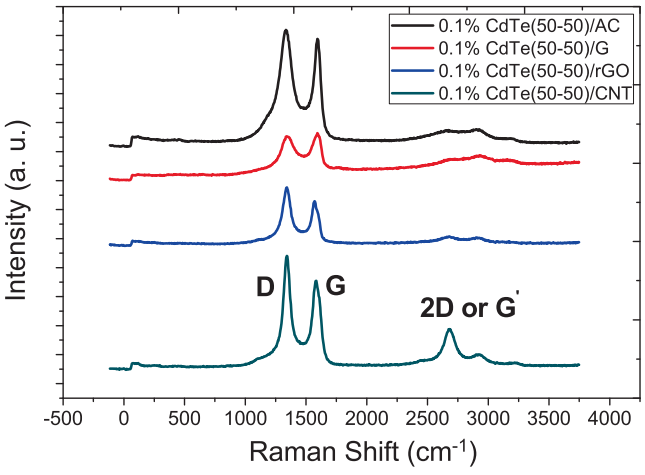

Fig. 2. Micro-Raman spectra of 0.1% CdTe(50–50)/AC, G, rGO, CNT catalysts.

3. Results and discussion

3.1. 1. Physical characterization

XRD analysis was realized to determine the crystal phase components of the catalysts. XRD patterns of 0.1 % CdTe(50–50) catalysts supported with different support materials were given in Fig. 1. The diffraction peaks of AC, G, rGO, CNT supported-CdTe(50–50) catalysts can be attributed as C (002) corresponding about 2θ = 24.8°, 22.8°, 24.5°, 25.6°, respectively. Furthermore, the diffraction peaks at approximately 43° corresponded to C (100) (JCPDS: 96-101-1061) [36]. The wide diffraction peak of graphene at 2θ = 11.5° can be assigned to graphene oxide [37]. The diffraction peaks at 53°, 66.9°, and 78.4° (2θ) for the 0.1 % CdTe(50–50)/CNT catalyst can be attributed to (400), (311), and (511) for cubic CdTe (JCPDS: 15–0770), respectively [38].

Micro-Raman spectroscopy was used to examine the structure, defect levels, and crystal behavior of the support materials AC, G, rGO, and CNT. Fig. 2 presents the Micro-Raman spectroscopy of supported-CdTe(50–50) catalysts. As can be shown from Fig. 2, all analyzed carbon materials had the characteristic D (~1350 cm^{-1}) and G (~1582 cm^{-1}) bands found in most other carbon materials [39]. The G band is common to all carbon structures with sp^2. However, the D band reveals the existence of disorder in the structure of carbon materials such as graphene [40]. The ratio (I_D/I_G) of the intensity of the D-Raman peak (I_D) and the G-Raman peak (I_G) can be used to measure the level of disorder in carbon materials. The calculated I_D/I_G ratios of CdTe/AC, CdTe/G, CdTe/rGO, and CdTe/CNT catalysts are 1.02,

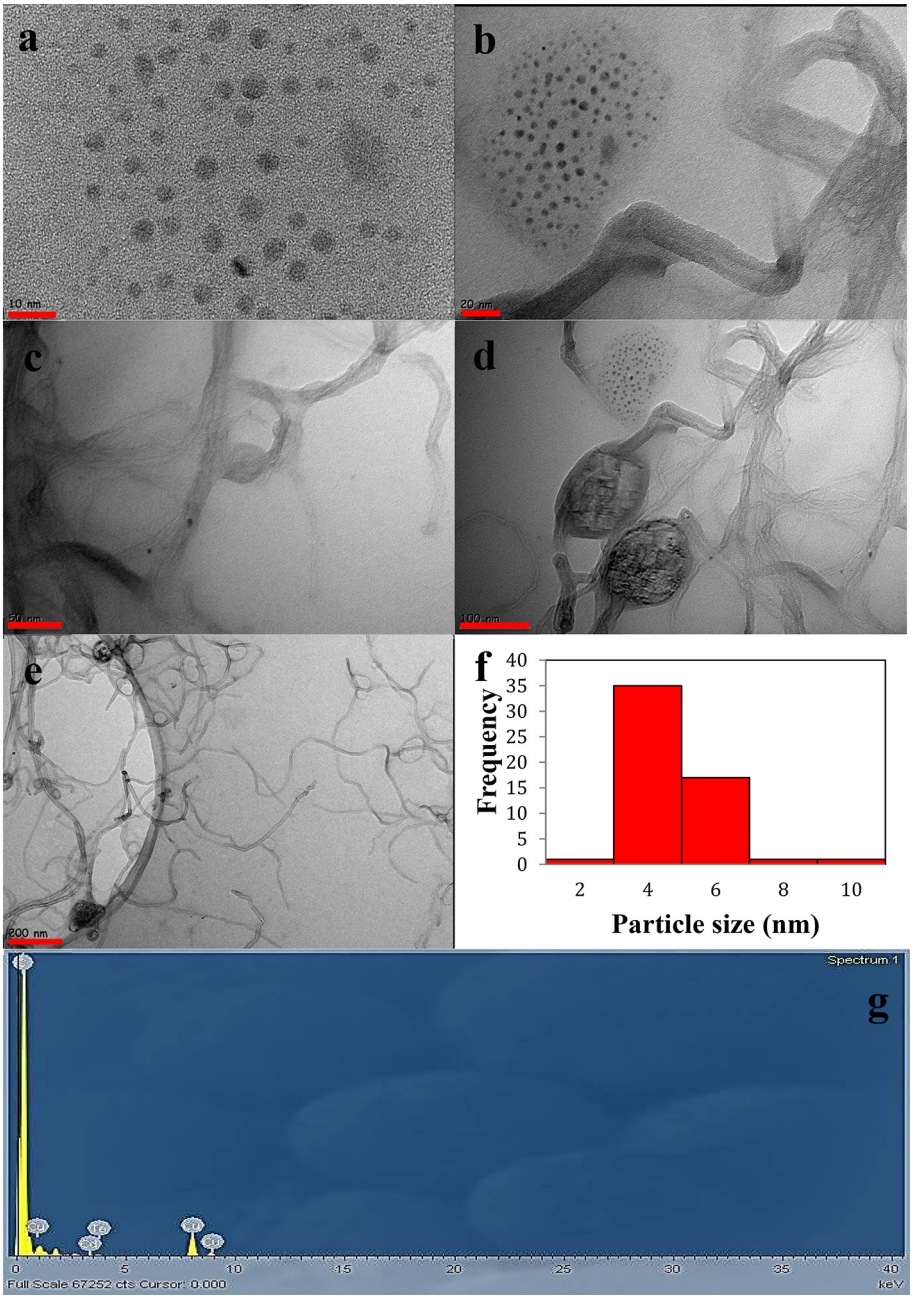

Fig. 3. TEM images of 0.1 % CdTe(50–50)/CNT catalyst (a) 10 nm, (b) 20 nm, (c) 50 nm, (d) 100 nm, (e) 200 nm, (f) 10 nm particle size distribution, and (g) EDS analysis.

0.99, 1.05, and 1.11, respectively. The high I_D/I_G ratio of the CdTe/CNT catalyst compared to the others clearly shows the defective nature of CdTe/CNT due to its porous structure [41].

The TEM-EDS images of 0.1 % CdTe(50–50)/CNT catalyst were given in Fig. 3. It could be observed from Fig. 3(a-e), the particles didn't form agglomeration and were generally homogeneously dispersed. Fig. 3f demonstrates the histogram and particle size of the 10 nm image. Particle size was found as about 3.7 nm. Many studies reported that it was emphasized that the activity increased with the reduction of particle size [42,43]. EDS results revealed the presence of Cd, Te, and C particles.

Fig. 4(a-d) displays the possible chemical states of Cd and Te in the 0.1 % CdTe(50–50)/CNT catalyst defined by using XPS analysis. In all XPS results, peak positions were determined relative to C 1s at a binding energy of 284.6 eV. The C 1s of two different chemical shifts components with the binding energy of 284.8 and 288.2 eV could be attributed to C—C and O-C═O [44]. In addition, the binding energy of 531.1 eV in the O 1s spectrum corresponds to the C═O bond [45]. The binding energy at 405.5 eV and 412.4 eV of Cd 3d (Fig. 4c) have two peaks at $3d_{5/2}$ and $3d_{3/2}$, which shows the possible formation of CdO which are consistent with the values noticed for Cd^{2+} [46,47]. Fig. 4d demonstrates the binding energies of Te 3d. The binding energies at 577 eV and 585 eV corresponded to Te $3d_{5/2}$ and Te $3d_{3/2}$ at the Te–O bond formation peak from oxidation of Te^{4+} species [48]. Furthermore, two weak peaks at 572 eV and 581 eV in the Cd-Te bond indicate that the CdTe surface is composed of $CdTeO_x$ and CdTe [49].

The TPR, TPO, and TPD analyses of CdTe(50–50)/CNT catalyst was examined to investigate the behavior during the reduction, oxidation, and desorption with hydrogen, oxygen, and ammonia, respectively. These analyses were given in Fig. 5a-c. H_2-TPR analysis can ensure knowledge about the interplay between CdTe and CNT due to the effects on the catalytic performance and properties of the catalyst when CNT interacts with the metal [50]. TPR profiles show the reduction behavior of metal oxides of catalysts. The reduction peak of CNT starts at approximately 500 °C. As emphasized in many studies, the high peak at 667 °C can be attributed to CNT [51–53]. The reduction peak formed at 380 °C can be assigned to the Cd-O or Te-O metal oxide originating from CdTe. Metal oxide presence was observed in the TPR analysis, as in the XPS analysis. The O_2-TPO analysis of 0.1 % CdTe (50–50)/CNT catalyst was demonstrated in Fig. 5b. TPO analysis is a material characterization process that is heated to a specific temperature by passing an oxidizing gas mix including oxygen on the sample and then can form oxidation in the thermal excitation that occurs. It could be seen from Fig. 5b that 0.1 % CdTe(50–50)/CNT catalyst has sharp peak TPO profiles at 586 °C. When it was doped with Cd and Te metals, it was seen that the metals are oxidized before the support material and the oxidation temperature decreases due to the metal support contact [54]. It has been reported in the literature that the oxidation peak for CNT occurs between 600 and 700 °C [55]. TPD analysis is utilized to define the adsorption sites on the sample with an inert gas mixture of gases such as NH_3 and CO_2, which examines the events happening on the surface of solid samples and whose temperature is modified via a temperature program. This analysis primarily involves measuring the rate of adsorption from the sample surface at low temperatures with a known gas and inert gas mixture, and the rate of desorption as the temperature increases [56]. The NH_3-TPD curves of 0.1 % CdTe(50–50)/CNT catalyst was illustrated in Fig. 5c. TPD curves change the acidic state of the sample as a weak acid, medium acid, and strong acid as the temperature increases [57,58]. It could be observed from Fig. 5c that the NH_3 desorption profile of the 0.1 %CdTe(50–50)/CNT catalyst offers two different desorption peaks.

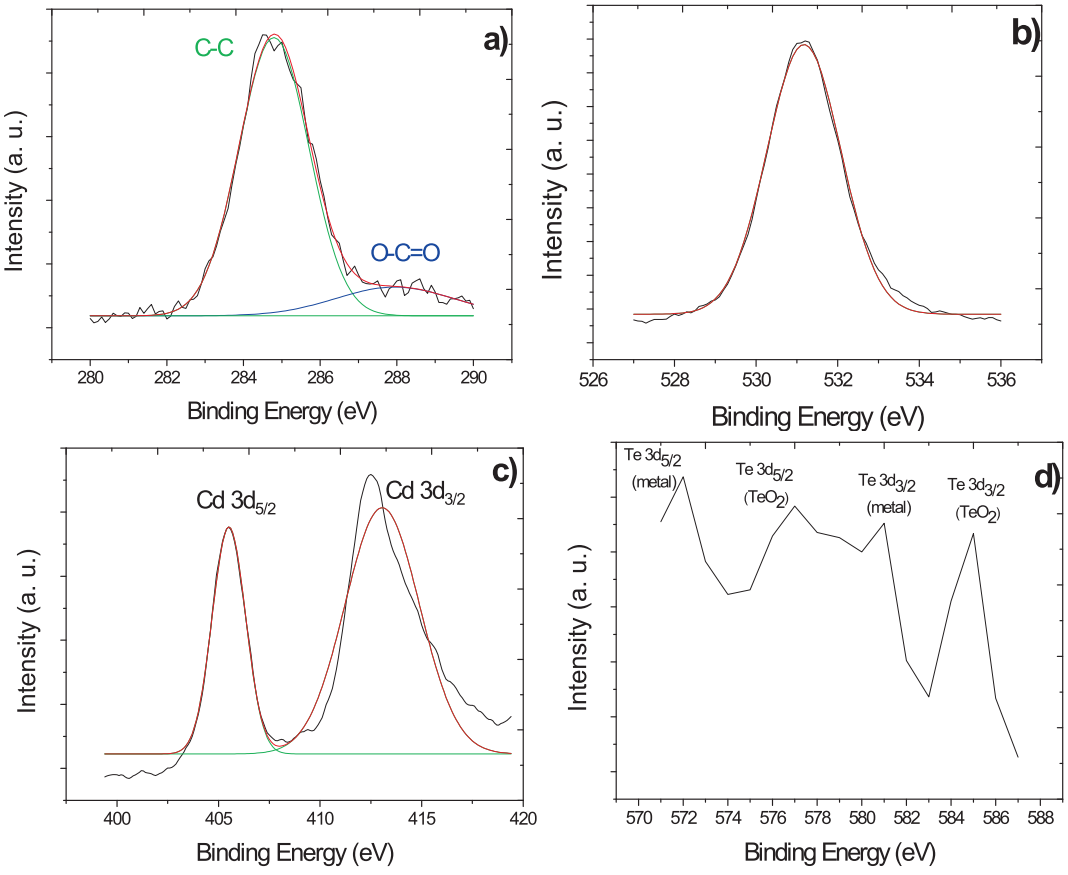

Fig. 4. XPS spectra of (a) C 1s, (b) O 1s, (c) Cd 3d, (e) Te 3d for 0.1 % CdTe(50–50)/CNT catalyst.

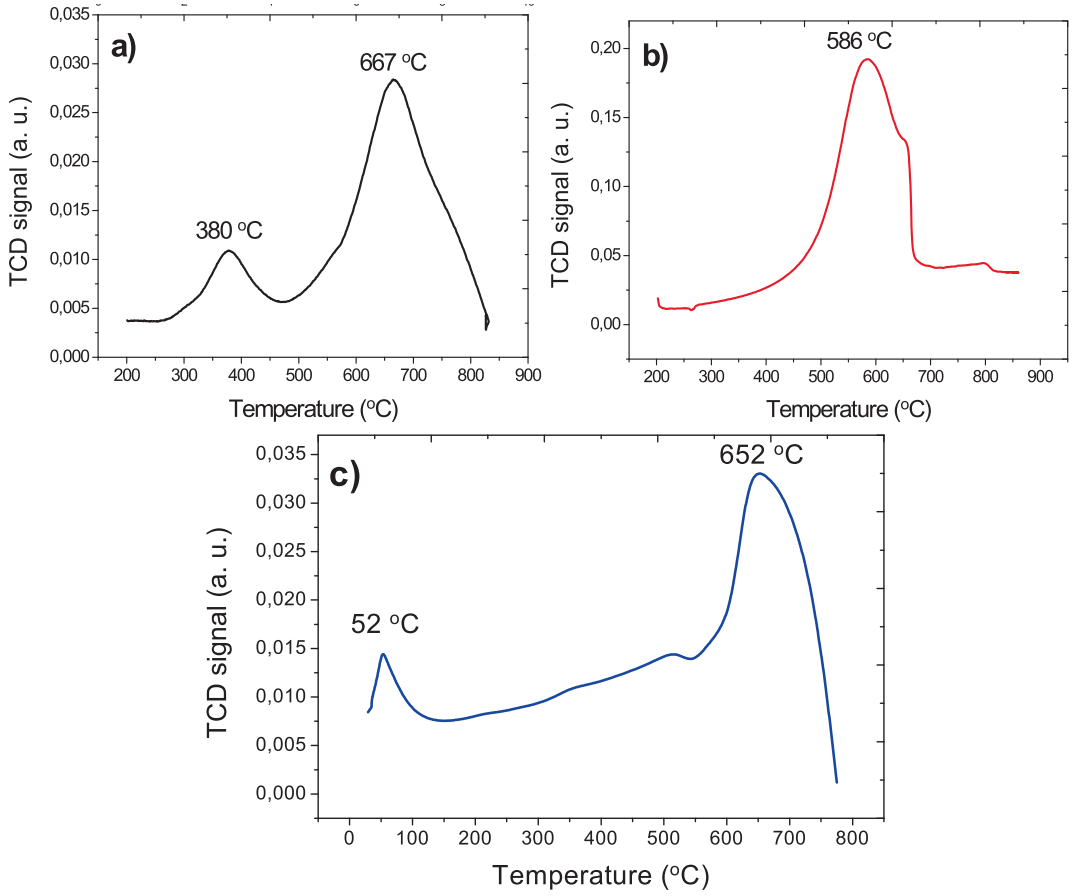

Fig. 5. H_2-TPR a), O_2-TPO b), and NH_3-TPD c) profiles of CdTe(50–50)/CNT catalyst.

These peaks were observed at 52 °C assigned to weak acid sites and the other NH_3 desorption peak at high temperature 652 °C originating from strong acid sites. Since NH^{4+} ions fixed to Brønsted acid sites are more unstable than the NH_3 molecular bond at Lewis acid sites, it can be predicted that the desorption peak at low temperature (52 °C) removes NH^{4+} ions bound to Brønsted acid sites. The desorption peak obtained at a higher temperature (652 °C) is related to the NH_3 molecule originating from Lewis acid sites [59].

4. 2. Electrochemical measurements of supported-CdTe catalysts

The CV, CA, and EIS analyses were used to examine electrochemical properties towards photocatalytic glucose electrooxidation of AC, G, GO-NH_2, rGO, and CNT supported-CdTe catalysts. These analyses were performed to both dark and under UV illumination to measure the catalytic activity, stability, and resistance of the catalysts in 1 M KOH + 0.5 M glucose solution. Fig. 6(a-c) shows the glucose electrooxidation taken without UV illumination of catalysts. The electrochemical behaviors of supported-CdTe catalysts were performed by CV analysis at between −0.65 and 0.65 V potential a scan rate of 100 mV/s. Although glucose has a high energy density, it is a difficult fuel to break down. Therefore, the catalysts were evaluated over the total current because oxidation peaks did not occur in glucose electrooxidation measurements. It could be observed from Fig. 6a and b that the 0.1 % CdTe(50–50)/CNT catalyst exhibited the best catalytic activity compared to the other catalysts. Fig. 6c indicates a comparison of 0.1 % CdTe(50–50)/CNT catalyst with 1 M KOH and 1 M KOH + 0.5 M glucose. The difference occurring in the total current is the catalytic activity originating from glucose. Moreover, the analyses of these catalysts under UV illumination are given in Fig. 7a-d. The 0.1 % CdTe(50–50)/CNT catalyst exhibited better catalytic activity with the specific activity of 2.57 mA/cm^2 under UV illumination compared to other catalysts and dark (1.9 mA/cm^2). Fig. 7c indicates CV analyses under UV illumination of 0.1 % Cd/CNT, 0.1 % Te/CNT, and 0.1 % CdTe(50–50)/CNT catalysts. The 0.1 % CdTe(50–50)/CNT catalyst displayed higher photocatalytic activity under UV illumination compared to 0.1 % Cd/CNT (1.89 mA/cm^2) and 0.1 % Te/CNT (0.94 mA/cm^2) catalysts. It can be thought that the reason why 0.1 % CdTe(50–50)/CNT catalyst has higher catalytic activity compared to 0.1 % Cd/CNT and 0.1 % Te/CNT catalysts provides much better activity due to the synergistic effects provided by the alloy nanostructure and higher tolerance against poisoning effect [29,60]. The stability of the 0.1 % CdTe(50–50)/CNT catalyst was examined during 30 cycles by CV analysis (Fig. 7d). It was observed that although there was a rapid decrease during the first 10 cycles, afterward it gradually stabilized.

CA analysis was performed to measure the stability and poison resistance of CdTe(50–50)/AC, G, rGO, CNT catalysts. Fig. 8(a-d) indicates the CA curves of catalysts. CA analysis of 0.1 % CdTe(50–50)/CNT catalyst were performed at different potentials (0.1 V, 0.3, and 0.6 V) under UV illumination (Fig. 8a). CA analysis at 0.6 V potential exhibited the best resistance and stability. After 1000 s, 0.1 % CdTe (50–50)/CNT catalyst was better activity and stability compared to other catalysts under UV illumination at 0.6 V potential (Fig. 8b). It could be seen from Fig. 8c that the 0.1 % CdTe(50–50)/CNT catalyst taken under UV illumination was more stable than received in the dark. As in the CV results, 0.1 % CdTe(50–50)/CNT catalyst exhibited the best activity and stability compared to the dark and other catalysts.

Fig. 9(a-c) presents the Nyquist plots obtained from the EIS analysis to examine the electrocatalytic resistance of the 0.1 % CdTe(50–50)/

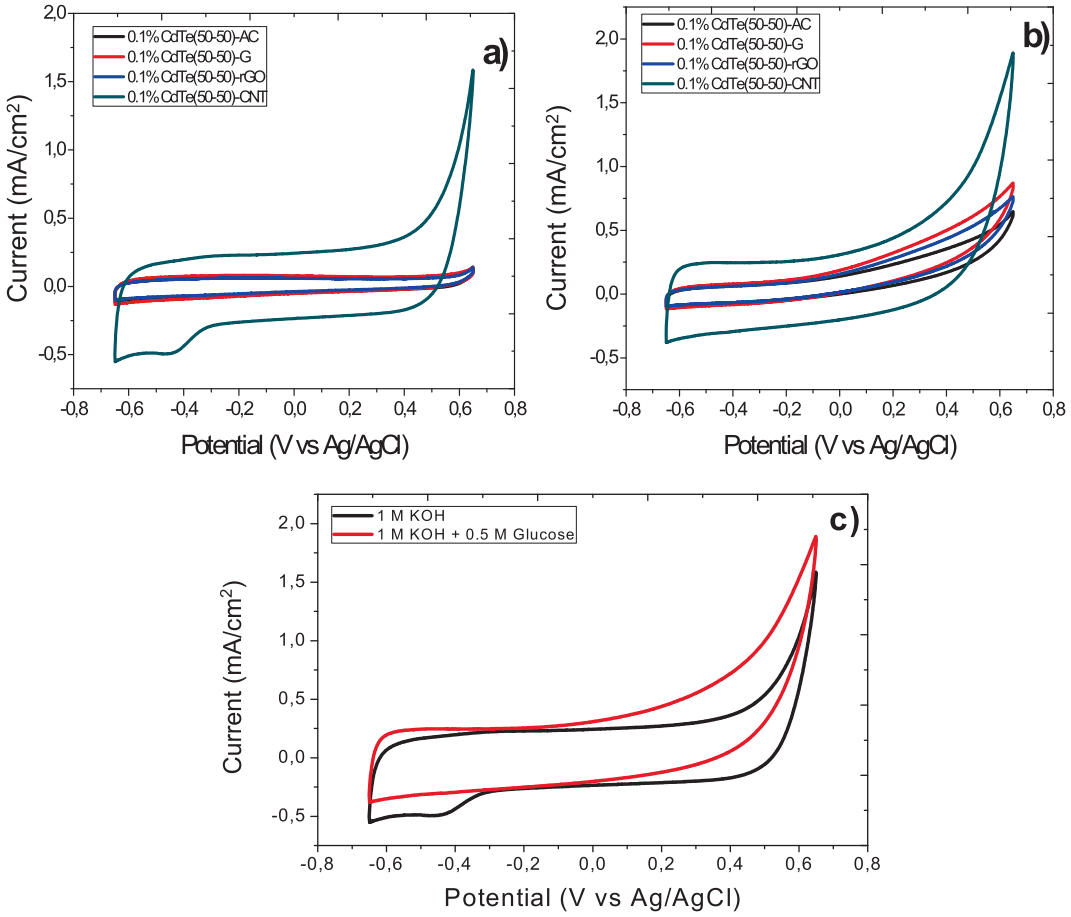

Fig. 6. Cyclic voltammograms of 0.1 % CdTe(50–50)/AC, G, GO-NH_2, rGO, CNT catalysts in (a) 1 M KOH, (b) 1 M KOH + 0.5 M $C_6H_{12}O_6$, and (c) both solution comparison of CdTe(50–50)/CNT catalyst at 100 mV/s scan rate.

AC, G, rGO, CNT catalysts. These plots are usually known as semicircles, where the electrocatalytic resistance increases as the diameter of the circle decrease [61,62]. The charge transfer resistance (R_{ct}) is associated with the diameter of the semicircle because as the diameter decreases, R_{ct} decreases, and so the catalytic activity increases [63]. Fig. 9a demonstrates the Nyquist plots of the 0.1 % CdTe(50–50)/CNT taken under UV illumination in different potentials (0.1 V, 0.3 V, and 0.6 V). As seen in Fig. 9a, the Nyquist plot taken at the potential of 0.6 V exhibited the best photocatalytic activity. It could be clearly seen from Fig. 9b that the R_{ct} can be listed as follows; 0.1 % CdTe(50–50)/G > 0.1 % CdTe(50–50)/rGO > 0.1 % CdTe (50–50)/AC > 0.1 % CdTe(50–50)/CNT. The 0.1 % CdTe(50–50)/CNT catalyst has the highest carrier transfer performance because it has the lowest semicircular shape and charge transfer resistance compared to other catalysts. Furthermore, the carrier transfer performance was higher as the R_{ct} (161.8 Ω) value under UV illumination was lower compared to dark (414.2 Ω) (Fig. 9c).

5. Conclusion

The sodium borohydride reduction (SBH) method was used to prepare activated carbon (AC), graphene (G), reduced graphene oxide, carbon nanotube-supported CdTe catalyst. The XRD, Micro-Raman, TEM, XPS, and TPx (TPR, TPO, and TPD) analyses were realized to characterize these catalysts. XRD results revealed that carbon materials were formed and cubic CdTe structures were formed. According to the Micro-Raman results, the high level of I_D/I_G for CdTe/CNT, which indicates the disorder level in carbon materials, indicates that the CNT is defective due to its porous structure. TEM-EDS results demonstrated that CNT and CdTe metal particles were formed. In addition, it was observed that CdTe particles had a particle size of 3.7 nm and were homogeneously dispersed. XPS analysis illustrated that the electronic state and crystal structure of the catalyst have changed. TPR, TPO, and TPD analyses presented positive or negative shifts in the reduction, oxidation, and adsorption–desorption peaks of CNT when the temperature increased when doped with metal, indicating the presence of metal. The CV, CA, and EIS analyses were performed to the activity, stability, and resistance for photocatalytic glucose electrooxidation measurements of 0.1 % CdTe/AC, G, rGO, CNT catalysts in the dark and under UV illumination, respectively. The 0.1 % CdTe (50–50)/CNT catalyst under UV illumination displayed the best photocatalytic activity with a specific activity of 2.57 mA/cm^2 than both the dark (1.9 mA/cm^2) and other catalysts. Furthermore, it indicated the best stability and resistance for photocatalytic glucose electrooxidation by CA and EIS analyses under UV illumination as in the CV analysis. It was observed that 0.1 % CdTe(50–50)/CNT catalyst under UV illumination had a faster electron transfer rate and higher catalytic activity during photocatalytic glucose electrooxidation with the best stability and lowest Rct (161.8 Ω) value compared to dark (414.2 Ω). The 0.1 % CdTe(50–50)/CNT catalyst showed that it would be an important catalyst for photocatalytic fuel cells with its low metal content when compared to the literature.

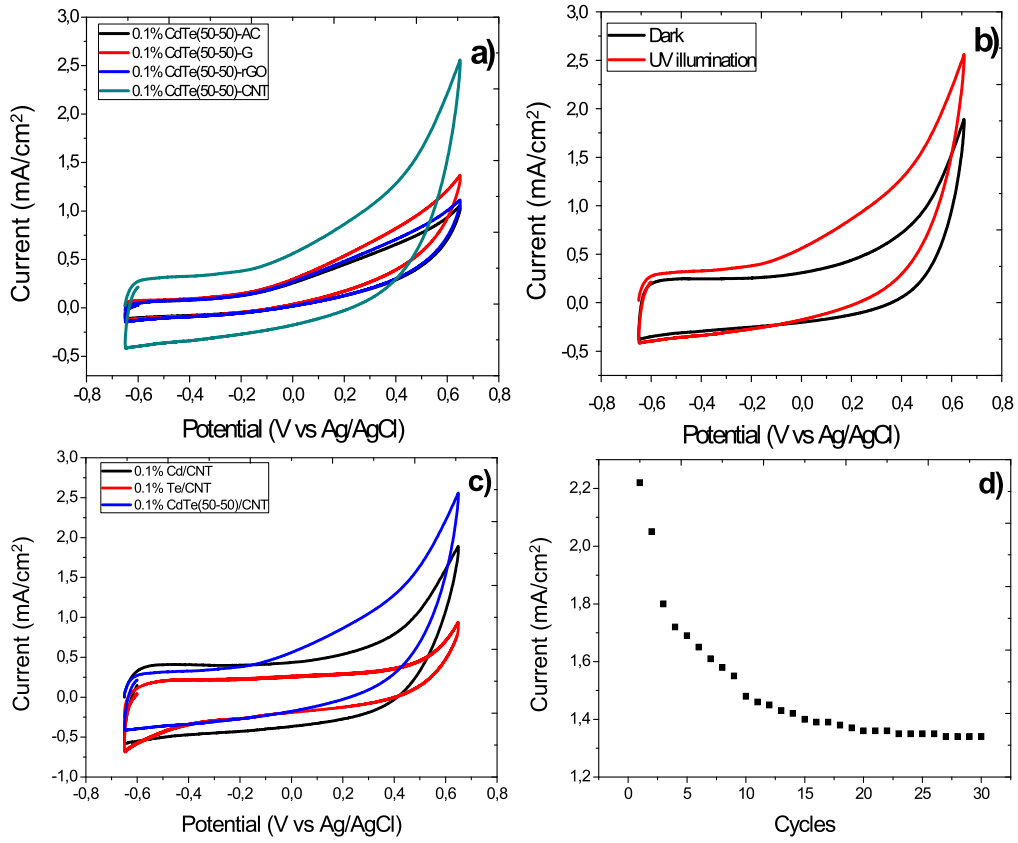

Fig. 7. Cyclic voltammograms of (a) 0.1 % CdTe(50–50)/AC, G, rGO, CNT catalysts under UV illumination, (b) dark and UV illumination comparison of CdTe (50–50)/CNT catalyst, (c) the comparison of 0.1 % Cd/CNT, 0.1 % Te/CNT, and 0.1 % CdTe(50–50)/CNT catalysts under UV illumination, and (d) stability of 0.1 % CdTe(50–50)/CNT catalyst under UV illumination at 100 mV/s scan rate in 1 M KOH + 0.5 M $C_6H_{12}O_6$ solution.

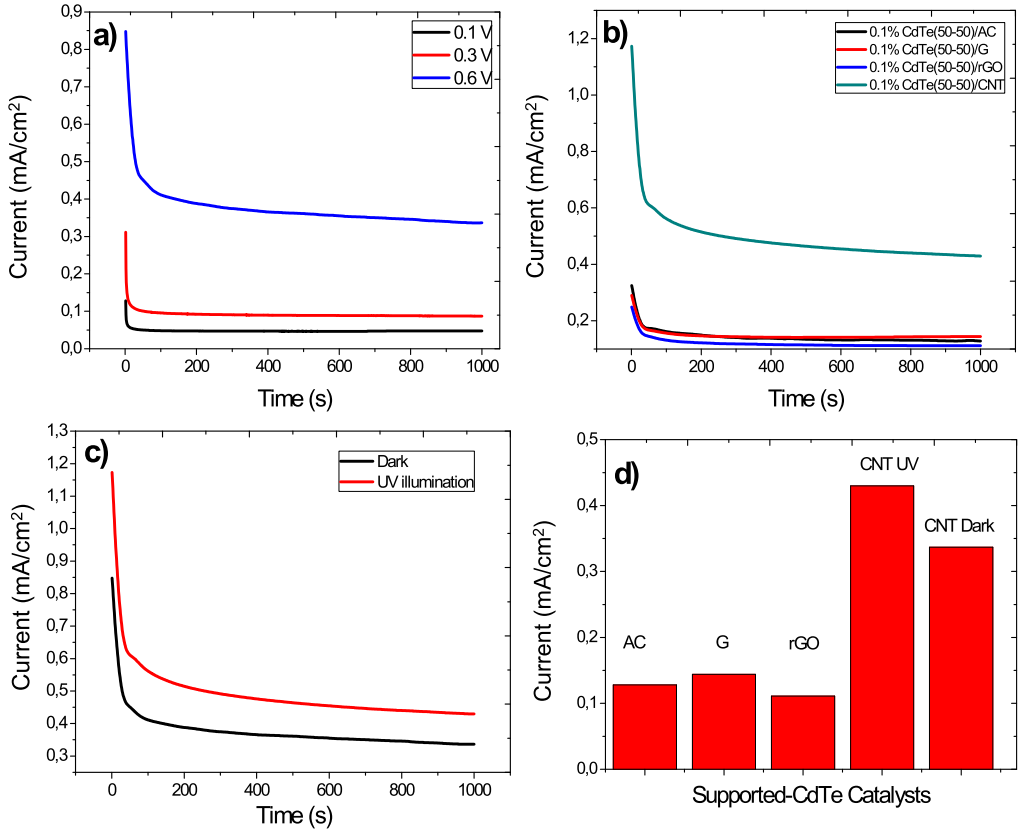

Fig. 8. CA curves of (a) 0.1 % CdTe(50–50)/CNT under UV illumination at 0.1 V, 0.3 V, and 0.6 V potentials, (b) 0.1 % CdTe(50–50)/AC, G, rGO, CNT catalysts under UV illumination at 0.6 V, (c) 0.1 % CdTe(50–50)/CNT dark and under UV illumination at 0.6 V, (d) specific activities after 1000 s in 1 M KOH + 0.5 M $C_6H_{12}O_6$ solution.

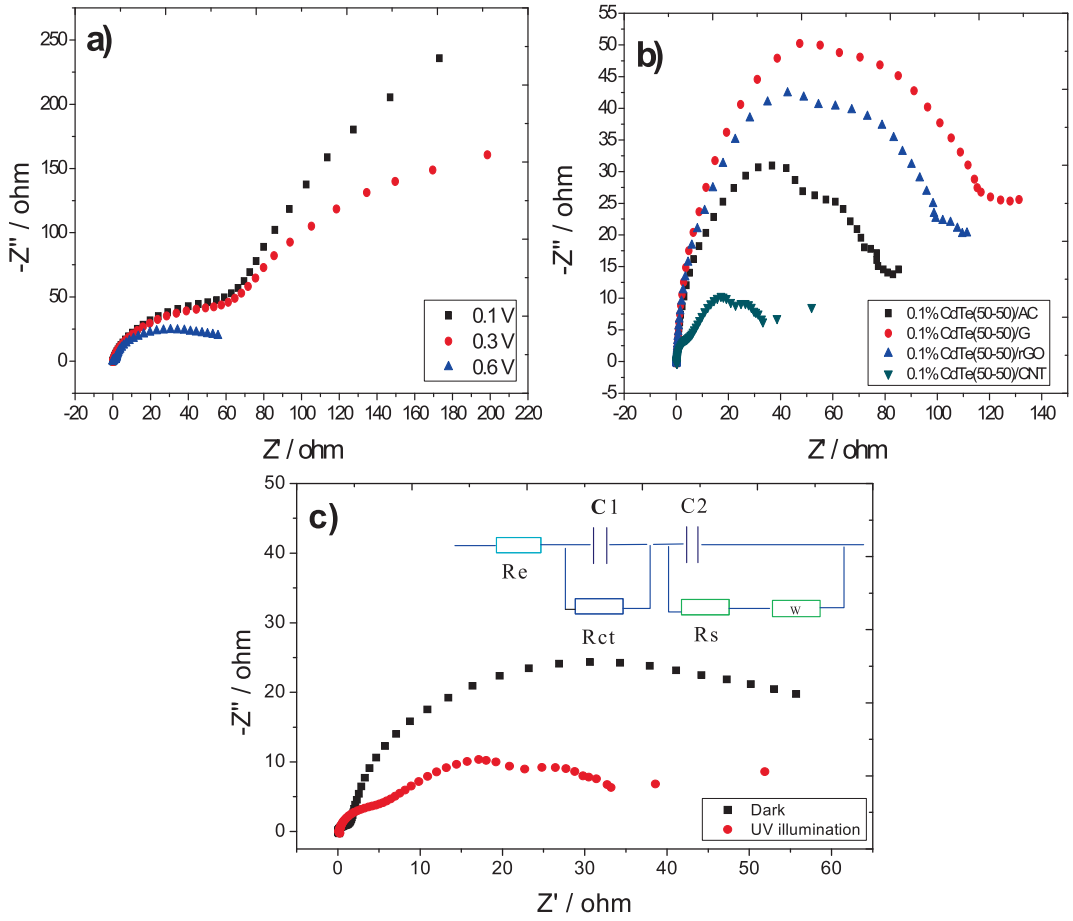

Fig. 9. Nyquist plots of (a) 0.1 % CdTe(50–50)/CNT in 0.1 V, 0.3 V, and 0.6 V potentials (under UV illumination), (b) 0.1 % CdTe/AC, G, rGO, CNT catalysts at 0.6 V (under UV illumination), (c) 0.1 % CdTe(50–50)/CNT catalyst both at dark and under UV illumination at 0.6 V in 1 M KOH + 0.5 M $C_6H_{12}O_6$ solution.

Declaration of Competing Interest

The authors declare that they have no known competing financial interests or personal relationships that could have appeared to influence the work reported in this paper.

References

[1] S.A. Asongu, M.O. Agboola, A.A. Alola, F.V. Bekun, The criticality of growth, urbanization, electricity and fossil fuel consumption to environment sustainability in Africa, Sci. Total Environ. 712 (2020) 136376.

[2] A. Eshghi, M. Kheirmand, Graphene/Ni–Fe layered double hydroxide nano composites as advanced electrode materials for glucose electro oxidation, Int. J. Hydrogen Energy 42 (2017) 15064–15072.

[3] A. Caglar, H. Kivrak, Highly active carbon nanotube supported PdAu alloy catalysts for ethanol electrooxidation in alkaline environment, Int. J. Hydrogen Energy 44 (2019) 11734–11743.

[4] X. Chen, F. He, Y. Shen, Y. Yang, H. Mei, S. Liu, T. Mori, Y. Zhang, Effect of carbon supports on enhancing mass kinetic current density of Fe-N/C electrocatalysts, Chem.–A Eur. J. 23 (2017) 14597–14603.

[5] T. Zhao, Q. Zhou, Y. Lv, D. Han, K. Wu, L. Zhao, Y. Shen, S. Liu, Y. Zhang, Ultrafast condensation of carbon nitride on electrodes with exceptional boosted photocurrent and electrochemiluminescence, Angew. Chem. Int. Ed. 59 (2020) 1139–1143.

[6] N. Karjule, R. Phatake, M. Volokh, I. Hod, M. Shalom, Solution-processable carbon nitride polymers for photoelectrochemical applications, Small Methods 3 (2019) 1900401.

[7] X. Li, G. Wang, L. Jing, W. Ni, H. Yan, C. Chen, Y.-M. Yan, A photoelectrochemical methanol fuel cell based on aligned TiO2 nanorods decorated graphene photoanode, Chem. Commun. 52 (2016) 2533–2536.

[8] L. Han, S. Guo, M. Xu, S. Dong, Photoelectrochemical batteries for efficient energy recovery, Chem. Commun. 50 (2014) 13331–13333.

[9] Q. Zhao, Z. Li, Q. Deng, L. Zhu, S. Luo, H. Li, Paired photoelectrocatalytic reactions of glucose driven by a photoelectrochemical fuel cell with assistance of methylene blue, Electrochim. Acta 210 (2016) 38–44.

[10] A. Caglar, D. Düzenli, I. Onal, I. Tezsevin, O. Sahin, H. Kivrak, A comparative experimental and density functional study of glucose adsorption and electrooxidation on the Au-graphene and Pt-graphene electrodes, Int. J. Hydrogen Energy 45 (2020) 490–500.

[11] A. Caglar, D. Düzenli, I. Onal, I. Tezsevin, O. Sahin, H. Kivrak, A novel experimental and density functional theory study on palladium and nitrogen doped few layer graphene surface towards glucose adsorption and electrooxidation, J. Phys. Chem. Solids 150 (2021) 109684.

[12] A. Caglar, B. Ulas, O. Sahin, H. Demir Kivrak, Few-layer graphene coated on indium tin oxide electrodes prepared by chemical vapor deposition and their enhanced glucose electrooxidation activity, Energy Storage 1 (2019) e73.

[13] K. Elouarzaki, A. Le Goff, M. Holzinger, J. Thery, S. Cosnier, Electrocatalytic oxidation of glucose by rhodium porphyrin-functionalized MWCNT electrodes: application to a fully molecular catalyst-based glucose/O2 fuel cell, J. Am. Chem. Soc. 134 (2012) 14078–14085.

[14] A. Brouzgou, S. Song, P. Tsiakaras, Carbon-supported PdSn and Pd3Sn2 anodes for glucose electrooxidation in alkaline media, Appl. Catal. B: Environ. S158–159 (2014) 209–216.

[15] S. Ghosh, Y. Holade, H. Remita, K. Servat, P. Beaunier, A. Hagège, K.B. Kokoh, T. W. Napporn, One-pot synthesis of reduced graphene oxide supported gold-based nanomaterials as robust nanocatalysts for glucose electrooxidation, Electrochim. Acta 212 (2016) 864–875.

[16] A. Caglar, N. Aktas, H. Kivrak, Tailoring cadmium composition on titanium dioxide to achieve enhanced photocatalytic glucose fuel cell anode performance, ACS Appl. Energy Mater. 4 (2021) 12298–12309.

[17] A. Caglar, H. Kivrak, N. Aktas, A.O. Solak, Fabrication of carbon-doped titanium dioxide nanotubes as anode materials for photocatalytic glucose fuel cells, J. Electron. Mater. (2021) 1–12.

[18] A. Caglar, H. Kivrak, N. Aktas, The effect of titanium dioxide-supported CdSe photocatalysts enhanced for photocatalytic glucose electrooxidation under UV illumination, Int. J. Hydrogen Energy 47 (2022) 21130–21145.

[19] A. Devadoss, P. Sudhagar, C. Ravidhas, R. Hishinuma, C. Terashima, K. Nakata, T. Kondo, I. Shitanda, M. Yuasa, A. Fujishima, Simultaneous glucose sensing and biohydrogen evolution from direct photoelectrocatalytic glucose oxidation on robust Cu2O–TiO2 electrodes, Phys. Chem. Chem. Phys. 16 (2014) 21237–21242.

[20] Y. Yan, J. Fang, Z. Yang, J. Qiao, Z. Wang, Q. Yu, K. Sun, Photoelectrochemical oxidation of glucose for sensing and fuel cell applications, Chem. Commun. 49 (2013) 8632–8634.

[21] A.R. Hamad, H. Calis, A. Caglar, H. Kivrak, A. Kivrak, Indole-based novel organic anode catalyst for glucose electrooxidation, Int. J. Energy Res. 46 (2022) 1659–1671.
[22] O.F. Er, A. Caglar, H. Kivrak, Enhanced electrochemical glucose oxidation in alkaline solution over indium decorated carbon supported palladium nanoparticles, Mater. Chem. Phys. 254 (2020) 123318.
[23] L. Yan, A. Brouzgou, Y. Meng, M. Xiao, P. Tsiakaras, S. Song, Efficient and poison-tolerant PdxAuy/C binary electrocatalysts for glucose electrooxidation in alkaline medium, Appl. Catal. B 150–151 (2014) 268–274.
[24] Y. Gu, H. Yang, B. Li, J. Mao, Y. An, A ternary nanooxide NiO-TiO2-ZrO2/SO42− as efficient solid superacid catalysts for electro-oxidation of glucose, Electrochim. Acta 194 (2016) 367–376.
[25] M. Long, L. Tan, A.D. Tang, The effects of electroplating conditions on the morphology and glucose oxidation performance of Cu2O/TiO2, Adv. Mater. Res. 937 (2014) 3–8.
[26] E. Antolini, Structural parameters of supported fuel cell catalysts: The effect of particle size, inter-particle distance and metal loading on catalytic activity and fuel cell performance, Appl. Catal. B 181 (2016) 298–313.
[27] E. Antolini, Carbon supports for low-temperature fuel cell catalysts, Appl. Catal. B 88 (2009) 1–24.
[28] A. Galińska, J. Walendziewski, Photocatalytic water splitting over Pt − TiO2 in the presence of sacrificial reagents, Energy Fuels 19 (2005) 1143–1147.
[29] A. Caglar, B. Ulas, M.S. Cogenli, A.B. Yurtcan, H. Kivrak, Synthesis and characterization of Co, Zn, Mn, V modified Pd formic acid fuel cell anode catalysts, J. Electroanal. Chem. 850 (2019) 113402.
[30] B. Ulas, A. Caglar, S. Yılmaz, U. Ecer, Y. Yilmaz, T. Sahan, H. Kivrak, Towards more active and stable PdAgCr electrocatalysts for formic acid electrooxidation: The role of optimization via response surface methodology, Int. J. Energy Res. 43 (2019) 8985–9000.
[31] O.F. Er, A. Caglar, B. Ulas, H. Kivrak, A. Kivrak, Novel carbon nanotube supported Co@Ag@Pd formic acid electrooxidation catalysts prepared via sodium borohydride sequential reduction method, Mater. Chem. Phys. 241 (2020) 122422.
[32] Z. Ma, J. Liu, Y. Zhu, Y. Zhao, H. Lin, Y. Zhang, H. Li, J. Zhang, Y. Liu, W. Gao, S. Li, L. Li, Crystal-facet-dependent catalysis of anatase TiO2 on hydrogen storage of MgH2, J. Alloy. Compd. 822 (2020) 153553.
[33] M. Akdemir, T. Avci Hansu, A. Caglar, M. Kaya, H. Demir Kivrak, Ruthenium modified defatted spent coffee catalysts for supercapacitor and methanolysis application, Energy Storage 3 (2021) e243.
[34] P. Reeves, R. Ohlhausen, D. Sloan, K. Pamplin, T. Scoggins, C. Clark, B. Hutchinson, D. Green, Photocatalytic destruction of organic dyes in aqueous TiO2 suspensions using concentrated simulated and natural solar energy, Sol. Energy 48 (1992) 413–420.
[35] S. Pinilla, A. Machín, S.-H. Park, J.C. Arango, V. Nicolosi, F. Márquez-Linares, C. Morant, TiO2-based nanomaterials for the production of hydrogen and the development of lithium-ion batteries, J. Phys. Chem. B 122 (2018) 972–983.
[36] H. Soleimani, M.K. Baig, N. Yahya, L. Khodapanah, M. Sabet, B. Demiral, M. Burda, Impact of carbon nanotubes based nanofluid on oil recovery efficiency using core flooding, Results Phys. 9 (2018).
[37] R. Siburian, H. Sihotang, S. Raja, M. Supeno, C. Simanjuntak, New route to synthesize of graphene nano sheets, Orient. J. Chem. 34 (2018) 182–187.
[38] G. She, T. Cai, L. Mu, W. Shi, Template-free electrochemical synthesis of Cd/CdTe core/shell nanowires and CdTe nanotubes, CrystEngComm 22 (2020) 4301–4305.
[39] M.S. Dresselhaus, A. Jorio, M. Hofmann, G. Dresselhaus, R. Saito, Perspectives on carbon nanotubes and graphene raman spectroscopy, Nano Lett. 10 (2010) 751–758.
[40] L. Estevez, V. Prabhakaran, A.L. Garcia, Y. Shin, J. Tao, A.M. Schwarz, J. Darsell, P. Bhattacharya, V. Shutthanandan, J.-G. Zhang, Hierarchically porous graphitic carbon with simultaneously high surface area and colossal pore volume engineered via ice templating, ACS Nano 11 (2017) 11047–11055.
[41] T. Palaniselvam, H.B. Aiyappa, S. Kurungot, An efficient oxygen reduction electrocatalyst from graphene by simultaneously generating pores and nitrogen doped active sites, J. Mater. Chem. 22 (2012) 23799–23805.
[42] D.S. Kim, S.J. Han, S.-Y. Kwak, Synthesis and photocatalytic activity of mesoporous TiO2 with the surface area, crystallite size, and pore size, J. Colloid Interface Sci. 316 (2007) 85–91.
[43] C. Jiang, M. Wei, Z. Qi, T. Kudo, I. Honma, H. Zhou, Particle size dependence of the lithium storage capability and high rate performance of nanocrystalline anatase TiO2 electrode, J. Power Sources 166 (2007) 239–243.
[44] B. Sivaranjini, M. Rajkumar, C.P. Ganesh, S. Umadevi, Vertical alignment of liquid crystals over a functionalized flexible substrate, Sci. Rep. 8 (2018).
[45] F.G. Pacheco, A.A.C. Cotta, H.F. Gorgulho, A.P. Santos, W.A.A. Macedo, C.A. Furtado, Comparative temporal analysis of multiwalled carbon nanotube oxidation reactions: Evaluating chemical modifications on true nanotube surface, Appl. Surf. Sci. 357 (2015) 1015–1023.
[46] W. Li, M. Li, S. Xie, T. Zhai, M. Yu, C. Liang, X. Ouyang, X. Lu, H. Li, Y. Tong, Improving the photoelectrochemical and photocatalytic performance of CdO nanorods with CdS decoration, CrystEngComm 15 (2013) 4212–4216.
[47] Y.-S. Li, F.-L. Jiang, Q. Xiao, R. Li, K. Li, M.-F. Zhang, A.-Q. Zhang, S.-F. Sun, Y. Liu, Enhanced photocatalytic activities of TiO2 nanocomposites doped with water-soluble mercapto-capped CdTe quantum dots, Appl. Catal. B 101 (2010) 118–129.
[48] S. Sharma, S. Shivaprasad, S. Kohli, A. Rastogi, Substrate temperature dependence of electrical conduction in nanocrystalline CdTe: TiO2 sputtered films, Pure Appl. Chem. 74 (2002) 1739–1749.
[49] T. Ch, Low temperature ferromagnetic properties of CdS CdTe thin fi, Chin. Phys. B (2017).
[50] V.G. Deshmane, S.L. Owen, R.Y. Abrokwah, D. Kuila, Mesoporous nanocrystalline TiO2 supported metal (Cu Co, Ni, Pd, Zn, and Sn) catalysts: Effect of metal-support interactions on steam reforming of methanol, J. Mol. Catal. A: Chem. 408 (2015) 202–213.
[51] R.M.M. Abbaslou, J. Soltan, A.K. Dalai, Effects of nanotubes pore size on the catalytic performances of iron catalysts supported on carbon nanotubes for Fischer-Tropsch synthesis, Appl. Catal. A 379 (2010) 129–134.
[52] B. Igor, K. Yevhen, S. Peter, TPR study of core-shell Fe@ Fe 3 O 4 nanoparticles supported on activated carbon and carbon nanotubes, Adv. Mater. Phys. Chem. 2012 (2012).
[53] A.-R. Leino, M. Mohl, J. Kukkola, P. Mäki-Arvela, T. Kokkonen, A. Shchukarev, K. Kordas, Low-temperature catalytic oxidation of multi-walled carbon nanotubes, Carbon 57 (2013) 99–107.
[54] J. Van Doorn, M.A. Vuurman, P. Tromp, D. Stufkens, J. Moulijn, Correlation between Raman spectroscopic data and the temperature-programmed oxidation reactivity of coals and carbons, Fuel Process. Technol. 24 (1990) 407–413.
[55] L.M. Chew, W. Xia, H. Düdder, P. Weide, H. Ruland, M. Muhler, On the role of the stability of functional groups in multi-walled carbon nanotubes applied as support in iron-based high-temperature Fischer-Tropsch synthesis, Catal. Today 270 (2016) 85–92.
[56] P.J. Barrie, Analysis of temperature programmed desorption (TPD) data for the characterisation of catalysts containing a distribution of adsorption sites, Phys. Chem. Chem. Phys. 10 (2008) 1688–1696.
[57] M. Zhou, P. Liu, K. Wang, J. Xu, J. Jiang, Catalytic hydrogenation and one step hydrogenation-esterification to remove acetic acid for bio-oil upgrading: model reaction study, Catal. Sci. Technol. 6 (2016) 7783–7792.
[58] H.-J. Choi, J.-S. Kim, M. Kang, Photodecomposition of concentrated ammonia over nanometer-sized TiO∼ 2, V-TiO∼ 2, and Pt/V-TiO∼ 2 photocatalysts, Korean Chem. Soc 28 (2007).
[59] D. Zhang, L. Zhang, L. Shi, C. Fang, H. Li, R. Gao, L. Huang, J. Zhang, In situ supported MnO x–CeO x on carbon nanotubes for the low-temperature selective catalytic reduction of NO with NH 3, Nanoscale 5 (2013) 1127–1136.
[60] H. Ye, Y. Li, J. Chen, J. Sheng, X.-Z. Fu, R. Sun, C.-P. Wong, PdCu alloy nanoparticles supported on reduced graphene oxide for electrocatalytic oxidation of methanol, J. Mater. Sci. 53 (2018) 15871–15881.
[61] T.A. Hansu, A. Caglar, O. Sahin, H. Kivrak, Hydrolysis and electrooxidation of sodium borohydride on novel CNT supported CoBi fuel cell catalyst, Mater. Chem. Phys. 239 (2020) 122031.
[62] A. Caglar, M.S. Cogenli, A.B. Yurtcan, H. Kivrak, Effective carbon nanotube supported metal (M = Au, Ag Co, Mn, Ni, V, Zn) core Pd shell bimetallic anode catalysts for formic acid fuel cells, Renewable Energy 150 (2020) 78–90.
[63] B. Ulas, A. Caglar, O. Sahin, H. Kivrak, Composition dependent activity of PdAgNi alloy catalysts for formic acid electrooxidation, J. Colloid Interface Sci. 532 (2018) 47–57.